nature climate change

Article

https://doi.org/10.1038/s41558-022-01520-4

2021 North American heatwave amplified by climate change-driven nonlinear interactions

Received: 20 September 2021

Accepted: 7 October 2022

Published online: 24 November 2022

Check for updates

Samuel Bartusek [1,2] ✉, Kai Kornhuber [2,3] & Mingfang Ting [2]

Heat conditions in North America in summer 2021 exceeded previous heatwaves by margins many would have considered impossible under current climate conditions. Associated severe impacts highlight the need for understanding the physical drivers of the heatwave and relations to climate change, to improve the projection and prediction of future extreme heat risks. Here, we find that slow- and fast-moving components of the atmospheric circulation interacted, along with regional soil moisture deficiency, to trigger a 5-sigma heat event. Its severity was amplified ~40% by nonlinear interactions between its drivers, probably driven in part by land–atmosphere feedbacks catalysed by long-term regional warming and soil drying. Since the 1950s, global warming has transformed the peak daily regional temperature anomaly of the event from virtually impossible to a presently estimated ~200-yearly occurrence. Its likelihood is projected to increase rapidly with further global warming, possibly becoming a 10-yearly occurrence in a climate 2 °C warmer than the pre-industrial period, which may be reached by 2050.

Unprecedented heat conditions in the North American Pacific Northwest (PNW) in late June and early July 2021 affected millions of people, probably led to deaths in the thousands and promoted wildfires affecting air quality throughout the continent. Centers for Disease Control (CDC) records suggest hundreds of excess deaths in both Washington and Oregon states during the heatwave, with hundreds more in British Columbia officially attributed to heat, probably undercounting the true toll[1–3]. Heat-related emergency room visits spiked, totalling nearly 3,000 during 25–30 June in the US PNW[4]. The high vulnerability of the affected region to extreme heat amplified its dangers: air conditioning access in the Seattle and Portland metropolitan areas is among the lowest in the country[5], while many PNW counties have among the largest outdoor agricultural worker populations and highest social vulnerability in the country[6]. Exacerbated by drought conditions (covering 95% of the US PNW by 22 June 2021[7]), wildfires sparked during and following the heatwave constituted some of 93 large fires, contributing to millions of acres of the western United States being burned by August 2021[8]. Wildfire smoke caused particulate matter pollution across the continent, for instance contributing to the worst air quality in 15 years in New York City[9].

Even as global warming increases the severity and frequency of heatwaves[10,11], the magnitude of this event exceeded what many may have considered plausible under current climate conditions[12]. While heat records are typically broken by small increments[13,14], this event shattered records by tens of degrees Celsius[15]. Such an unprecedented event[16] raises the pressing question of whether future projections of heat extremes are too conservative or their mechanisms inadequately captured by climate models. It is therefore important to understand the physical drivers of the event and assess their connections with climate change. From an attribution perspective, was this anomaly so extreme to be considered virtually impossible regardless of climate change (a 'black swan' event[17,18]) or was it plausible and foreseeable and even made more likely due to baseline warming (a 'grey swan'[19])? Further, were its drivers mechanistically altered by climate trends,

[1]Department of Earth and Environmental Sciences, Columbia University, New York, NY, USA. [2]Lamont-Doherty Earth Observatory, Columbia University, Palisades, NY, USA. [3]German Council on Foreign Relations, DGAP, Berlin, Germany. ✉e-mail: samuel.bartusek@columbia.edu

beyond their occurrence in a warming background—perhaps indicating exacerbated future risk?

Whether any change in atmospheric dynamics or land–atmosphere interaction is implicated in amplifying current and future heat extremes is a persistent question: common heatwave mechanisms may be modified by climate change beyond a shift in background conditions. Midlatitude heat extremes, typically triggered by anticyclonic circulation anomalies, have often been associated with persistently amplified planetary scale atmospheric waves[20–24]. Conditions favourable for wave amplification may become more frequent, possibly connected to weakening of the north–south temperature gradient[25–27]. Additionally, thermodynamic land–atmosphere feedbacks can strongly amplify heatwave temperatures, often involving nonlinear processes[28–32]. Land areas typically occupy two distinct regimes of soil–atmosphere interaction: areas where soil moisture is too high or too low for its variability to affect evapotranspiration, versus areas with 'transitional' climates (between wet and dry), where soil moisture variability affects evapotranspiration and therefore temperature[33]. The central United States is a noted transitional climate hotspot of strong soil moisture–temperature coupling[33,34] but, although the presently wet PNW is projected to dry due to warming[35–37] and aridification of other wet regions has been implicated in amplifying summer temperature variability (for example, central Europe[38]), the PNW has not garnered similar focus on land–atmosphere contributions to its temperature variability and their potential changes.

Unprecedented PNW heat conditions and contributing factors

In ERA5 reanalysis (Methods), anomalous near-surface temperatures during the PNW heatwave were accompanied by extremely high geopotential height and exceptionally low soil moisture. The regionally averaged 2-m temperature anomaly over land exceeded five times its daily standard deviation over 1981–2010, while geopotential height and soil dryness anomalies exceeded four and three times theirs (Fig. 1d). The PNW experienced at least 7 days exceeding the 99th percentile (over 1981–2010) in each of these variables (Supplementary Fig. 1). However, this analysis of a large region (40–60° N, 110–130° W), capturing the broad-scale meteorological factors influencing the event rather than focusing on its most severe hotspots, may understate local severity: in some areas, 9-day-averaged (25 June to 3 July) temperature exceeded 12 °C above normal.

The PNW was not the only anomalously hot region during this period: a hemisphere-wide pattern of anomalies extended from the land surface into the mid-atmosphere (Fig. 1a–c). Central Eurasia and northeastern Siberia both experienced warm anomalies, dry soils and high geopotential heights; the North Atlantic constituted a fourth region of high geopotential height. With alternating cool, wet and low-height regions, this pattern comprised a circumglobal wavenumber-4 disturbance (four peaks and troughs in each variable encircling the hemisphere; Extended Data Fig. 1), a pattern historically associated with North American wildfires[39]. A wavenumber-4 upper atmospheric circulation anomaly (Methods) was established since 19 June (before the heatwave) and strongly amplified (>1.5σ) since 21 June (Fig. 1d and Extended Data Fig. 1). Accordingly, in late June the jet stream assumed a persistent 'wavy' configuration with strong meridional wind meanders (Extended Data Fig. 1 and Supplementary Fig. 2)—exhibiting a zonal-mean wind and temperature fingerprint for amplified planetary scale waves that some evidence suggests may become more frequent with warming[25,26,40]. Further, convection in the western subtropical Pacific may have helped excite a late-June Rossby wavetrain extending towards North America that locked phase with the existing hemispheric wave, amplifying the geopotential height and temperature anomalies in the PNW and perhaps also strengthening the hemispheric wave (Extended Data Fig. 1), suggesting an important role for atmospheric dynamics in this event.

However, during the heatwave the PNW experienced markedly stronger temperature and height anomalies than other nodes of the hemispheric wave, despite similar soil moisture anomalies (compare Fig. 1b,c). Additionally, regional temperature continued rising during the event after geopotential height had peaked, mirroring the direction of soil moisture anomalies (Fig. 1d and Supplementary Fig. 1). These observations suggest a potential role for both shorter-term atmospheric dynamics (ref. [41] reveal an important contribution from upstream cyclogenesis leading to sudden blocking-induced heating aloft) and two-way land–atmosphere feedbacks in amplifying and prolonging the PNW heatwave.

Heat contributions from nonlinear interactions

Interactions in the land–atmosphere system probably intensified the heatwave, as a contributor to a ~3 °C nonlinear component (of the total ~10 °C peak regional mean heat anomaly) above the heat accounted for by long-term linear relations between driver variables (Fig. 2). The proximate causes of the heatwave were extreme anomalies in common heatwave drivers—high geopotential height (resulting from wave–wave interaction; Extended Data Fig. 1) and dry soil, which both exceeded their historical (1979–2020) ranges yet largely followed expected bivariate distribution relationships (Fig. 2a–c), as in simulated record-shattering heatwaves in similar regions[15]. However, the peak temperatures of the heatwave markedly exceeded the linear regressions of temperature against geopotential height or soil moisture (by 4–5 °C), which are otherwise strongly predictive (Fig. 2a,b). A multiple regression, incorporating their simultaneous anomalies, confirms nonlinear temperature amplification maximizing during the peak of the event at ~3 °C (increasing ~7 °C by ~40%), an ~3σ amplification (Fig. 2c,d). Temporally, this amplification term behaved out-of-phase with geopotential height but in-phase with soil moisture (it increased as soils continued to dry despite declining geopotential height; Figs. 2d and 1d and Supplementary Fig. 4), raising the possibility that two-way soil moisture–temperature interactions contributed to these nonlinearities.

From a spatial perspective, dryness across much of the region following a heatwave at the beginning of June persisted throughout June, even during cool periods, establishing potential preconditions for land–atmosphere feedbacks (Supplementary Fig. 5 and Fig. 1d). Ultimately, many of the highest temperature anomalies of the event were collocated with negative evaporative fraction anomalies (most notably in the region's interior plateaus, across eastern Washington and central British Columbia; warmer areas with more arid and Mediterranean continental climates), their convergence suggesting a region of potential feedback activity (Extended Data Fig. 2). We find that enhanced sensible and suppressed latent heat fluxes extended across many parts of the region and tended to correspond with increased warming relative to available radiative energy, versus areas with different flux partitioning (Extended Data Figs. 3 and 4). More quantitatively, an 850 hPa-level temperature budget reveals distinct evolutions and drivers of heating within different subregions (Extended Data Fig. 5). For example, adiabatic compression and horizontal advection contributed strongly to heating along the coastal ranges of British Columbia and immediately west of the Cascades, partially triggered by an offshore cut-off low-pressure system. However, overall, the residual term of the budget (which estimates diabatic heating, probably related in part to land–atmosphere processes) provided heating during the peak warming days of the heatwave and was ultimately the dominant driver in areas where 2-m temperature anomalies became most extreme—in the interior of the region, as the heatwave progressed eastward. This substantiates that, in addition to other processes, land–atmosphere interactions probably amplified the heating, especially where and when it was strongest (Extended Data Fig. 5), although further analysis is needed to link 850 hPa-level behaviour directly to surface processes. Meanwhile, many of the most extreme areas that plausibly experienced

https://doi.org/10.1038/s41558-022-01520-4

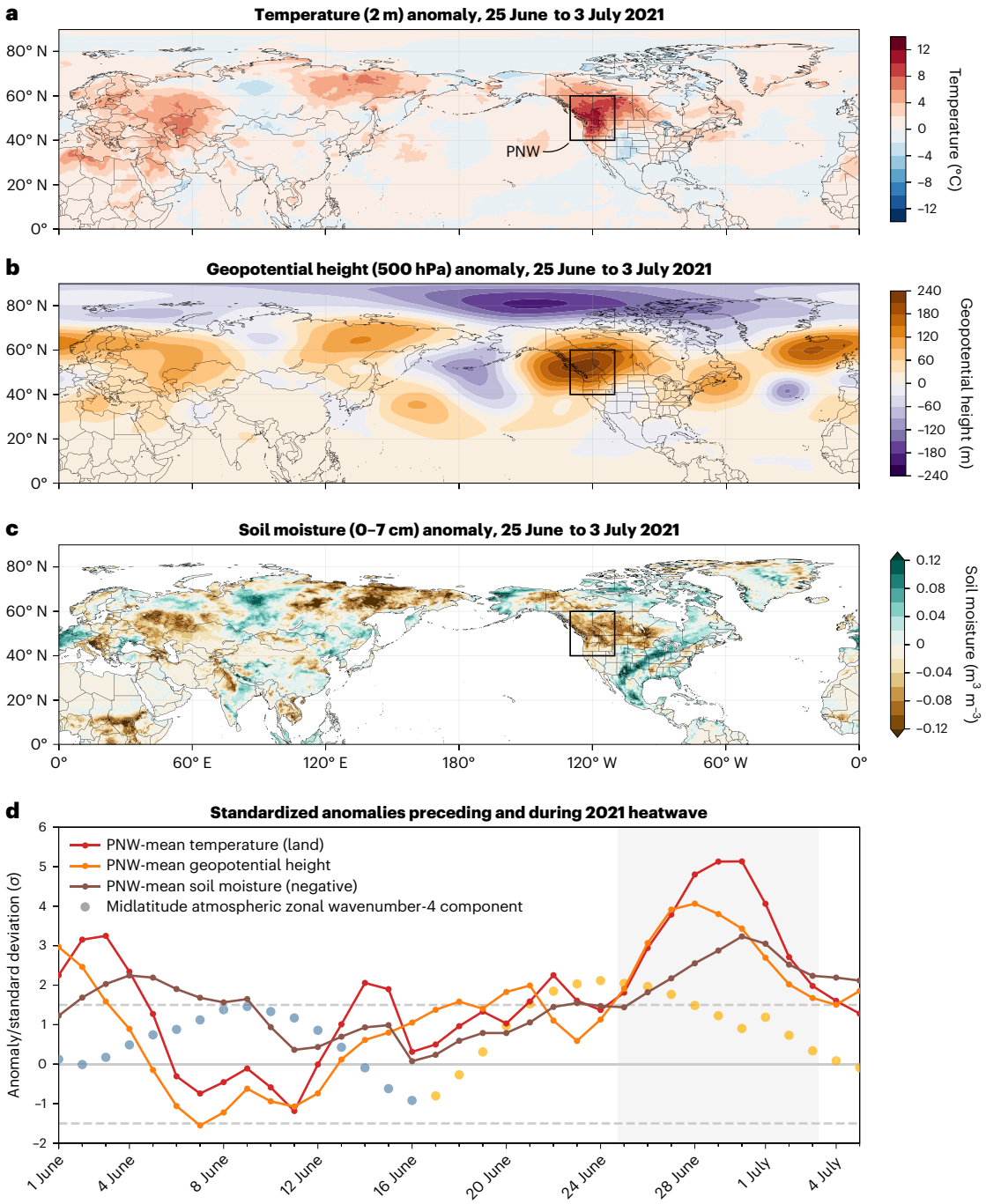

Fig. 1 | Timing and location of the PNW heatwave and its associated atmospheric dynamical and land surface conditions. a–d, Northern Hemisphere temperature (**a**), geopotential height (**b**) and soil moisture (**c**) anomalies during the 2021 PNW heatwave (25 June to 3 July) and their evolution throughout June averaged over the PNW (**d**) (black box in **a**–**c**; 40–60° N, 110–130° W; land temperature only). During the heatwave, much of the PNW experienced extreme anomalies in temperature, geopotential height and soil moisture exceeding 5, 4 and 3 standard deviations from their 1981–2010 means (dashed grey lines indicate ±1.5σ). Panel **d** also shows the amplitude of a zonal wavenumber-4 disturbance in the midlatitude upper atmospheric circulation, coloured blue when in negative phase and yellow in positive phase (Methods). This wave corresponds to four regions of positive (alternating with four negative) geopotential height anomalies encircling the hemisphere, visible in **a**–**c** with associated temperature and soil moisture anomalies, affecting central Eurasia, Northeastern Siberia, the PNW and the North Atlantic. See Extended Data Fig. 1 for a detailed perspective on the evolution of atmospheric dynamical aspects.

land–atmosphere temperature amplification have experienced multi-decadal summer drying, warming and increasing temperature variability (Extended Data Fig. 6; Conclusions).

Furthermore, ongoing trends favour the nonlinear regional-mean behaviour amplifying this heatwave—thus, while the extreme heat of 2021 was unprecedented, it was nevertheless mechanistically linked to historical regional climate change. First, the distributions of the driver variables have individually shifted towards 2021 conditions: late June–early July temperature, geopotential height and soil dryness increased over 1979–2020, with trends accelerating over 1991–2020 (Supplementary Figs. 6 and 7). Consequently, the largest historical extremes in these variables tend to occupy more recent years

https://doi.org/10.1038/s41558-022-01520-4

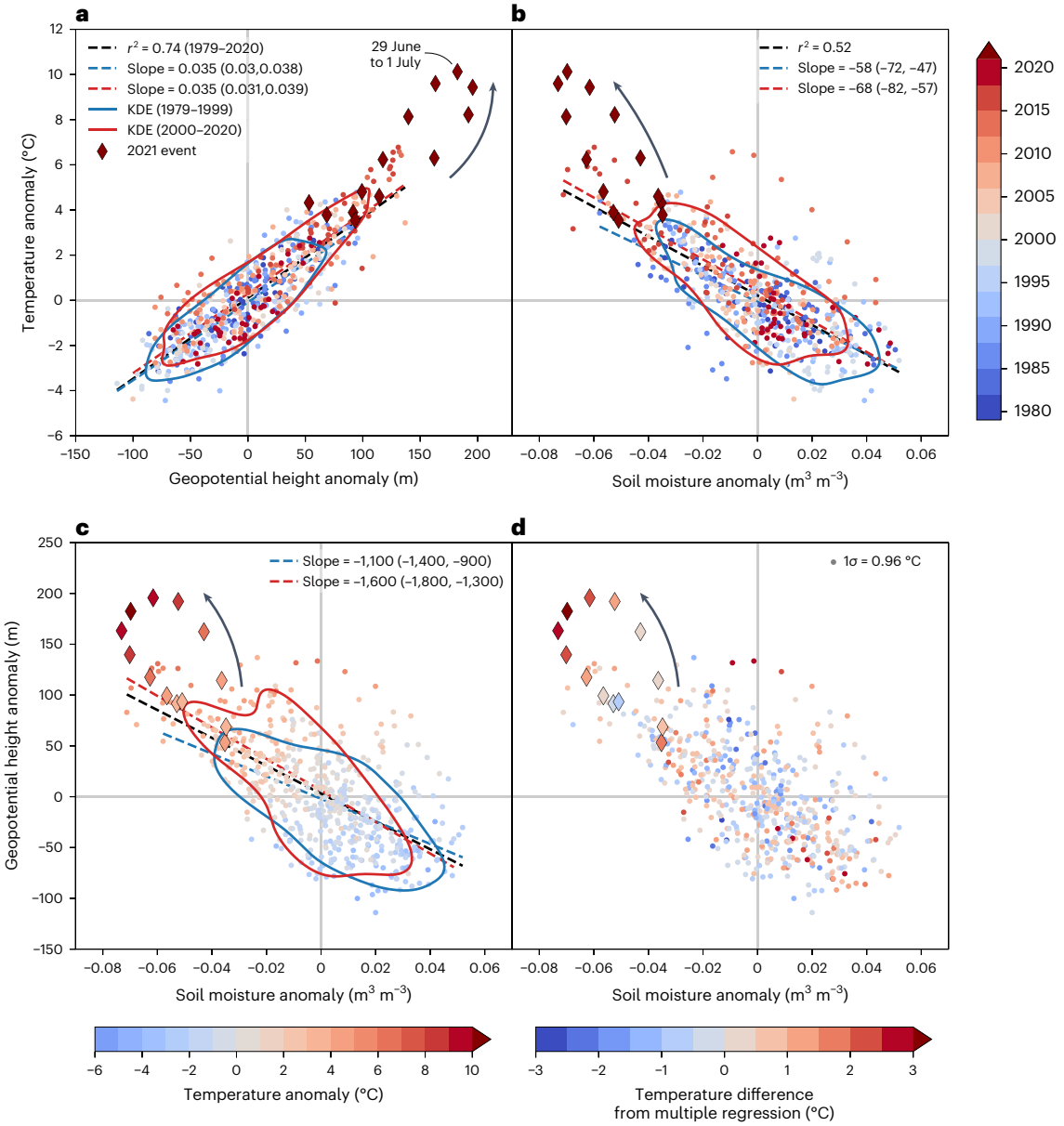

Fig. 2 | Nonlinear interactions of common drivers and their long-term trends. a, Three-day-running-averaged PNW-mean 2 m temperature versus 500 hPa geopotential height anomalies, centred on each day from 23 June to 5 July 1979–2020, coloured by year. Dark red diamonds show 2021 (temperature maximizing on 30 June); the arrow indicates their temporal evolution. The historical linear regression between the variables is in black. Blue and red dashed lines show regressions over 1979–1999 and 2000–2020, respectively, with 95% CIs provided in legends. Red and blue curves illustrate the 0.5 contour of a KDE of the two-dimensional distribution of the variables for each of the periods. **b**,**c**, Same as **a** but for soil moisture versus temperature anomalies (**b**) and soil moisture versus geopotential height anomalies (**c**); markers in **c** are coloured by temperature anomaly. **d**, Same as **c** but markers coloured by the difference between the observed temperature (colours in **c**) and predicted temperature for each soil moisture and geopotential height value pair by multiple linear regression (Supplementary Fig. 3), indicating that the highest temperatures of the event involved nonlinear contributions of ~3 °C out of a total ~10 °C anomaly.

(Fig. 2a,b). Second, bivariate distributions combining these variables have shifted towards high temperature and geopotential height and dry soils occurring simultaneously (Fig. 2a,b, visually comparing kernel density estimate (KDE) contours). Notably, historical extreme temperatures approaching 2021 conditions have also tended to be displaced above the linear driver regressions (Fig. 2a,b). Indeed, while bivariate distribution shifts have primarily followed their underlying regressions, the slopes describing the relationships of temperature and geopotential height against soil moisture have strengthened (with probability 71% and 98%, respectively, via bootstrapping), indicating magnified temperature and geopotential height anomalies relative to soil moisture anomalies (Fig. 2b,c). Temperature–height density contours also potentially suggest a changing relationship in the positive extremes of the distribution, despite the unchanging linear relation (Fig. 2a), suggesting a change specific to heatwave mechanisms. While these conclusions hold over all of June–July (Supplementary Fig. 4), we note that late June–early July has exhibited especially pronounced trends in these variables and their variabilities (Supplementary Fig. 7), perhaps reflecting an advancing summer onset[42].

Role of soil moisture in amplifying PNW temperature extremes

Using a model experiment tailored to evaluate the role of soil moisture in climate, we determine that in the PNW, soil moisture–atmosphere

https://doi.org/10.1038/s41558-022-01520-4

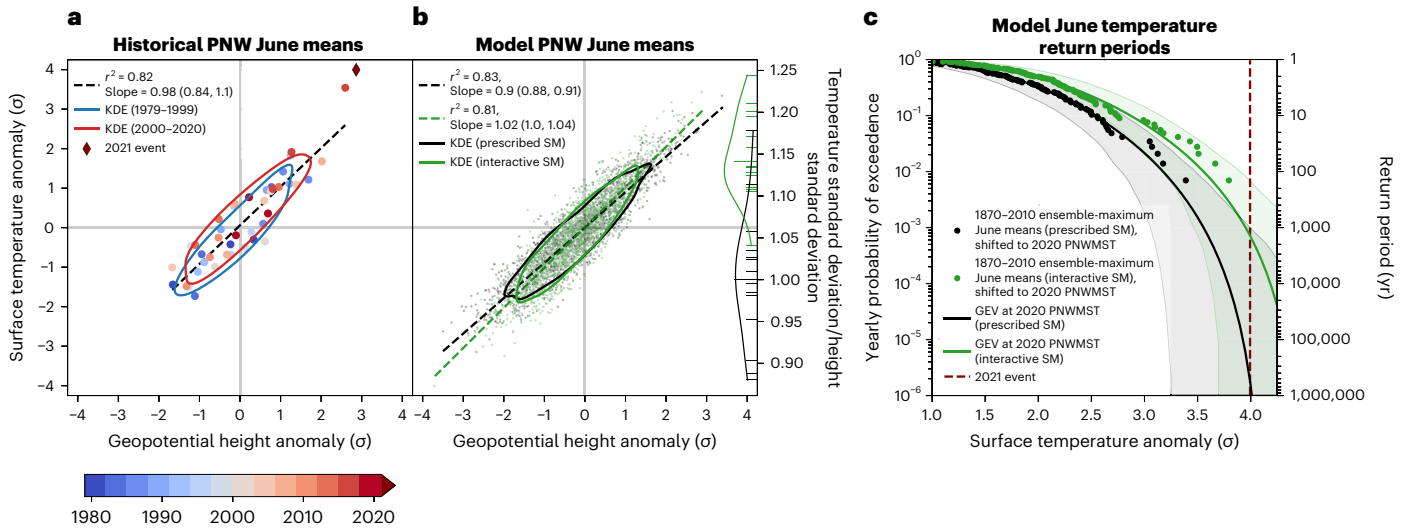

Fig. 3 | Modelled PNW monthly temperature variability and extreme event return periods, with versus without soil moisture interaction. a,**b**, June mean PNW-mean surface temperature versus 500 hPa geopotential height anomalies (standardized), from reanalysis (1979–2021) (**a**) and the CAM5–GOGA model experiment (1870–2010) (**b**), comparing prescribed (black) versus interactive (green) soil moisture (SM) ensembles. Regressions and KDE contours are as in Fig. 2 (but with 1.25× smoothing in **a** and showing the 0.3 contour in **b**). Panel **b** also compares (right *y* axis) the ratio of the temperature standard deviation of each member to the prescribed ensemble-total geopotential height standard deviation. Longer lines show ensemble-total ratios; curves show KDEs. **c**, Exceedance probability and return period as a function of standardized temperature anomaly for GEV distributions (curves, with bootstrapped 95% CIs shaded) fit to 1870–2010 ensemble-maximum June means and empirical return periods (dots). At present warming, the estimated return period for the June 2021 temperature anomaly (~4σ) is ~400-fold shorter with interactive soil moisture (~1,400-yearly versus ~500,000-yearly).

interactions probably make monthly scale temperature extremes of the magnitude of June 2021 many times more likely. We force a climate model with historical (1870–2010) sea surface temperatures, both with and without soil moisture interactivity (hereafter, interactive and prescribed ensembles) and we compare June mean surface temperature model output (2-m not available) against observations. We first confirm that the observed June mean 2021 surface temperature was extreme (Fig. 3a), with monthly temperature reaching ~4σ and exceeding its regression against geopotential height. In the model (standardized for comparison with observations; Methods), we find that soil moisture interaction significantly increases the ratio of monthly temperature variability versus geopotential height variability (by ~14%; Fig. 3b, right axis). Consistent with previous research[43], temperature variability increases modestly in interactive members, accompanying strongly increased mean temperature (Supplementary Fig. 8). Accordingly, the height–temperature regression slope across all member-months is significantly steeper in interactive members (by ~13%), while both lie within the confidence interval (CI) of the observed slope (Fig. 3b, left axis). However, this increase in the linear slope may underestimate changes toward the tails of the distribution, that is during extremes (Fig. 3b, KDE contours).

Consequently, the likelihood of the standardized temperature anomaly of June 2021 dramatically increases when soil moisture can interact with the atmosphere. We fit generalized extreme value (GEV) distributions to the yearly ensemble-maximum June mean temperature anomaly (Methods) of each ensemble, with their location parameters non-stationary in 5-year-smoothed annual PNW-mean surface temperature (PNWMST). We use PNWMST as a covariate instead of global mean surface temperature (GMST) to account for differing PNW-mean climate responses to global temperature between model configurations. Estimated empirical return periods are overlaid on the model curves, with each datapoint shifted in temperature by the dependence of the GEV location parameter on PNWMST. Fits and datapoints for each ensemble can thus be compared at a consistent baseline: at the observed PNWMST level of 2020, the GEV models estimate a ~400-fold increase (95% CI: 0.03–4,000,000) in the likelihood of the observed monthly anomaly of June 2021 between prescribed and interactive soil moisture ensembles, transforming it from an extremely unlikely ~500,000-yearly (~1,000–∞) event to a ~1,400-yearly (~150–∞) event. Overlaid empirical return periods suggest that GEV-derived return periods may conservatively estimate particularly severe events. Qualitatively similar results are found if 2- or 3-year GEV block sizes are used or if all June–August months are used instead of only June (not shown).

Increasing event likelihood driven by climate change

Recent climate change has rapidly increased the likelihood of the 2021 heatwave: over the past 70 years, such an event has multiplied in probability from virtually impossible to a multihundred-yearly event (Fig. 4). As above, we apply GEV analysis, a targeted approach for estimating extreme value statistics and an established method for attributing climate extremes to anthropogenic warming[44–46]. We note that assessing the probability of this event in temperature alone—despite its multivariate extreme characteristics—probably conservatively estimates its increasing likelihood as a compound event, given simultaneous trends in other variables such as soil moisture.

First, we note that the PNW has experienced not only shifting mean temperatures but also changing variability since 1979: daily mean June–July temperature anomalies have displayed positive and increasing skewness both regionally averaged (Supplementary Fig. 11) and across many within-region areas (Extended Data Fig. 6). While station-based daily-maximum and daily-minimum temperatures during June–August have shown small skewness in the PNW and not displayed strong historical increases[47], here we highlight an earlier summer period and daily mean temperatures. We further note that research has projected future modelled temperature skewness increases under CO_2 forcing in the PNW, probably linked to soil moisture interaction[48].

We apply GEV analysis to yearly-maximum June–August daily temperatures extending back to 1950, to maximize sample size and robustness, with both location and scale parameters non-stationary in 5-year-smoothed GMST (Methods). Results reveal drastic historical changes in heatwave probabilities: a hypothetical daily 8 °C regional temperature anomaly is estimated to have been virtually impossible in the 1950–1985 climate but has become an ~50-yearly event in the

https://doi.org/10.1038/s41558-022-01520-4

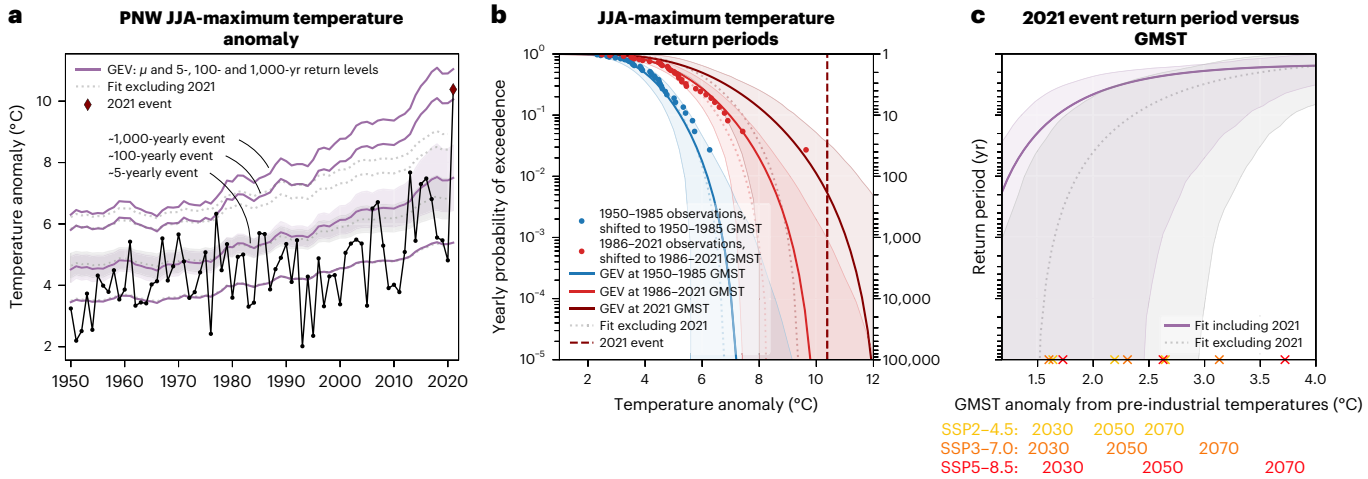

Fig. 4 | 2021 heatwave likelihood estimates over recent decades and under future emissions pathways. a, A GEV distribution fit to yearly June–August (JJA)-maximum daily-mean PNW-mean 2 m temperature overlaid on observations, both including (purple) and excluding (grey dotted) the event of 2021, plotting the location parameter (μ) and 5-, 100- and 1,000-year return period temperature levels (5-year return level bootstrapped 95% CI shaded). **b**, Return periods of temperature anomalies for historical periods 1950–1985 and 1986–2021 (fits are evaluated at and observations are shifted to the period-mean GMSTs) and for 2021 (finding a ~200-yearly return period), with bootstrapped 95% CIs shaded. **c**, GEV fits evaluated as a function of GMST, providing likelihood estimates for a future event analogous to the 2021 heatwave under different emission pathways (CMIP6 multimodel mean warming trajectories are displayed for reference). Future probabilities far exceed those estimated until today: the event may become a 10-yearly event before 2050 in even an intermediate emissions scenario (SSP 2–4.5).

climate since 1986 (Fig. 4b). Similarly, the 2021 heatwave (an ~10.4 °C peak anomaly, far exceeding the historical range) was virtually impossible even at the average global temperature over 1986–2021 (return period 95% CI: 1,500–∞) but by 2021 has become a ~200-yearly event (25–∞)—thereby experiencing an infinite increase in probability (at least ~13-fold). Its probability increase since 1950–1985 is likewise infinite (at least ~500,000-fold). Furthermore, the probability of an event exceeding the magnitude of 2021 will increase rapidly under further increasing GMST—projected to recur ~10-yearly before 2050 even at the warming of shared socioeconomic pathway SSP 2–4.5, a 'moderate' emissions scenario (before 2070 if excluding 2021 from the fit; Fig. 4c). Estimates using a stationary scale parameter are qualitatively similar but show lower event probabilities (Extended Data Fig. 7).

We fit GEV distributions to data both including the heatwave of 2021 as well as excluding it (Fig. 4). In including 2021, we follow refs. [45,46,49], assuming that the observation of 2021 is drawn from the same distribution as historical observations, since the study region was not selected solely to maximize local extremity but rather for a large-scale regional perspective, reducing (but not eliminating) selection bias. Alternatively, however, the excluding-2021 fit estimates a finite maximum possible temperature well below the 2021 observation even under current warming (Fig. 4b), questioning its validity. We note that the including-2021 fit is not rejected by a Kolmogorov–Smirnov test (Supplementary Figs. 9 and 10) despite its poor fit in similar analyses[46,49], which maintained a fixed scale parameter and analysed a smaller region more concentrated on the extreme. Ultimately, both fits underscore dramatic increases in heat-extreme probabilities resulting from gradual warming: in both, an ~1,000-yearly event in the 1950s would currently resemble an ~5-yearly event and has been surpassed many times (Fig. 4a). Furthermore, comparing future projections of a 2021-magnitude event, the fits roughly converge, both projecting <10-yearly recurrences by 2.5 °C GMST above pre-industrial temperatures. Notably, this threshold only increases to 2.75 °C GMST in a GEV fit with stationary instead of non-stationary scale parameters (Extended Data Fig. 7).

Conclusions

Given the extreme magnitude of the 2021 heatwave, an important question is whether it represents: a black swan event[17,18], effectively unforeseeable no matter the climate conditions; a grey swan event[19], made plausible by linking to common drivers and even more likely by background warming; or further, an event whose drivers do not act stationarily with respect to a moving background climate but are instead mechanistically altered by climate trends—with event likelihood thereby increasing beyond that induced by a background shift. We first find that, although the event of 2021 was unprecedented by large margins, it was traceable to common drivers, exhibiting extreme anomalies[15]. Interacting circulation features provided highly anomalous atmospheric dynamical forcing (4σ geopotential height exceedance) and land–atmosphere feedbacks probably amplified the severity of the event, contributing to a total ~40% nonlinear amplification. Further, however, we also find that the interactions amplifying this heatwave are mechanistically linked to trends in temperature, soil moisture and geopotential height that increase their likelihood, possibly suggesting a long-term shift in feedback behaviour underway in the region compounding background warming.

In contrast to first assessments of ref. [49] who concluded that the atmospheric dynamical patterns during this extreme were probably not exceptional, we provide evidence that the interaction of a persistent anomalous wavenumber-4 Rossby wave in the polar front jet and an atmospheric wave emanating from the Pacific probably played a key role in this extraordinary temperature anomaly (Fig. 1 and Extended Data Fig. 1). Further research is required to assess if the conditions for such waves are becoming more likely, for example by strengthened waveguidability[50] of the polar front jet due to amplified land warming at high latitudes[51,52] or increased convective activity in the western (and/or suppressed in the eastern) tropical Pacific[53].

Meanwhile, warming-forced midlatitude land drying[35,36] could shift wet regions, such as much of the PNW, towards a transitional climate between wet and dry, possibly strengthening land–atmosphere feedbacks and temperature variability[33]. However, the PNW has received little examination of shifting soil moisture–temperature coupling, even though some PNW areas already occupy transitional regimes during summer[54,55] and dry soil–heatwave linkages in the region are recognized[56]. Our findings suggest that rapid soil drying (particularly in early July, drying ~7% regionally between 1979–1999 and 2000–2020; Supplementary Fig. 7) may already be altering extreme

heat mechanisms: many of the anomalously hottest temperatures of the 2021 heatwave occurred in areas experiencing long-term decreasing evaporative fraction and increasing temperature variability (Extended Data Figs. 2 and 6). We additionally find increasing trends in four metrics of the terrestrial component of land–atmosphere coupling in many of the same areas since 1979 (Extended Data Fig. 6). Notably, land–atmosphere coupling and temperature variability increases are strongest where soil moisture is climatologically moderate instead of the driest areas—thus, in the PNW, drying may increase temperature variability more than in already arid regions like the southwestern United States[33]. In accordance with recent research demonstrating the emergence of heat-amplifying land–atmosphere feedbacks in regions not historically experiencing them[32] and, moreover, projections of widespread midcentury soil moisture regime shifts including the PNW[37], we suggest that the 2021 heatwave may represent an alarming manifestation of a shifting regime across much of the PNW from wet to transitional climate, making such events more likely through strengthened soil moisture–temperature coupling—however, further research is required to substantiate this.

Finally, our results underscore that even gradual warming over recent decades dramatically transformed the character of this extreme heat event. Since 1950, an anomaly of this magnitude has been refigured from virtually impossible to plausible and somewhat expected, with a return period of hundreds of years. Continued warming will cause the probability of an equal or stronger event to rapidly increase, potentially becoming an ~10-yearly occurrence with 2 °C warming above pre-industrial temperatures, which may be reached by 2050 in even a 'moderate' emissions scenario.

Online content

Any methods, additional references, Nature Research reporting summaries, source data, extended data, supplementary information, acknowledgements, peer review information; details of author contributions and competing interests; and statements of data and code availability are available at https://doi.org/10.1038/s41558-022-01520-4.

References

1. Popovich, N. & Choi-Schagrin, W. Hidden toll of the Northwest heat wave: hundreds of extra deaths. *The New York Times* (11 August 2021).
2. *Excess Deaths Associated with COVID-19* (CDC, 2021); https://www.cdc.gov/nchs/nvss/vsrr/covid19/excess_deaths.htm
3. *Heat-Related Deaths in B.C. Knowledge Update* (BC Coroners Service, accessed August 2021); https://www2.gov.bc.ca/assets/gov/birth-adoption-death-marriage-and-divorce/deaths/coroners-service/statistical/heat_related_deaths_in_bc_knowledge_update.pdf
4. Schramm, P. J. et al. Heat-related emergency department visits during the Northwestern heat wave—United States, June 2021. *MMWR Morb. Mortal. Wkly Rep.* **70**, 1020–1021 (2021).
5. *American Housing Survey (AHS)* (US Census Bureau, accessed August 2021); https://www.census.gov/programs-surveys/ahs.html
6. Tigchelaar, M., Battisti, D. S. & Spector, J. T. Work adaptations insufficient to address growing heat risk for U.S. agricultural workers. *Environ. Res. Lett.* **15**, 094035 (2020).
7. *Map Archive* (U.S. Drought Monitor, accessed August 2021); https://droughtmonitor.unl.edu/Maps/MapArchive.aspx
8. *National Fire News* (NICF, accessed August 2021); https://www.nifc.gov/fire-information/nfn
9. Silverman, H., Guy, M. & Sutton, J. Western wildfire smoke is contributing to New York City's worst air quality in 15 years. *CNN* (21 July 2021); https://edition.cnn.com/2021/07/21/weather/us-western-wildfires-wednesday/index.html
10. Meehl, G. A. & Tebaldi, C. More intense, more frequent, and longer lasting heat waves in the 21st century. *Science* **305**, 994–997 (2004).
11. Perkins-Kirkpatrick, S. E. & Lewis, S. C. Increasing trends in regional heatwaves. *Nat. Commun.* **11**, 3357 (2020).
12. Philip, S. Y. et al. *Rapid Attribution Analysis of the Extraordinary Heatwave on the Pacific Coast* (World Weather Attribution, 2021); https://www.worldweatherattribution.org/wp-content/uploads/NW-US-extreme-heat-2021-scientific-report-WWA.pdf
13. Coumou, D. & Robinson, A. Historic and future increase in the global land area affected by monthly heat extremes. *Environ. Res. Lett.* **8**, 034018 (2013).
14. Power, S. B. & Delage, F. P. D. Setting and smashing extreme temperature records over the coming century. *Nat. Clim. Change* **9**, 529–534 (2019).
15. Fischer, E. M., Sippel, S. & Knutti, R. Increasing probability of record-shattering climate extremes. *Nat. Clim. Change* **11**, 689–695 (2021).
16. Thompson, V. et al. The 2021 western North America heat wave among the most extreme events ever recorded globally. *Sci. Adv.* **8**, eabm6860 (2022).
17. Taleb, N. N. *The Black Swan: The Impact of the Highly Improbable* (Random House, 2007).
18. Aven, T. On the meaning of a black swan in a risk context. *Saf. Sci.* **57**, 44–51 (2013).
19. Lin, N. & Emanuel, K. Grey swan tropical cyclones. *Nat. Clim. Change* **6**, 106–111 (2015).
20. Petoukhov, V., Rahmstorf, S., Petri, S. & Schellnhuber, H. J. Quasiresonant amplification of planetary waves and recent Northern Hemisphere weather extremes. *Proc. Natl Acad. Sci. USA* **110**, 5336–5341 (2013).
21. Petoukhov, V. et al. Role of quasiresonant planetary wave dynamics in recent boreal spring-to-autumn extreme events. *Proc. Natl Acad. Sci. USA* **113**, 6862–6867 (2016).
22. Screen, J. A. & Simmonds, I. Amplified mid-latitude planetary waves favour particular regional weather extremes. *Nat. Clim. Change* **4**, 704–709 (2014).
23. Kornhuber, K. et al. Summertime planetary wave resonance in the Northern and Southern Hemispheres. *J. Clim.* **30**, 6133–6150 (2017).
24. Kornhuber, K. et al. Amplified Rossby waves enhance risk of concurrent heatwaves in major breadbasket regions. *Nat. Clim. Change* **10**, 48–53 (2019).
25. Mann, M. E. et al. Influence of anthropogenic climate change on planetary wave resonance and extreme weather events. *Sci. Rep.* **7**, 45242 (2017).
26. Mann, M. E. et al. Projected changes in persistent extreme summer weather events: the role of quasi-resonant amplification. *Sci. Adv.* **4**, eaat3272 (2018).
27. Kornhuber, K. & Tamarin-Brodsky, T. Future changes in northern hemisphere summer weather persistence linked to projected arctic warming. *Geophys. Res. Lett.* **48**, e2020GL091603 (2021).
28. Hirschi, M. et al. Observational evidence for soil-moisture impact on hot extremes in southeastern Europe. *Nat. Geosci.* **4**, 17–21 (2010).
29. Miralles, D. G., van den Berg, M. J., Teuling, A. J. & de Jeu, R. A. M. Soil moisture–temperature coupling: a multiscale observational analysis. *Geophys. Res. Lett.* **39**, L21707 (2012).
30. Miralles, D. G., Teuling, A. J., van Heerwaarden, C. C. & Vilà-Guerau de Arellano, J. Mega-heatwave temperatures due to combined soil desiccation and atmospheric heat accumulation. *Nat. Geosci.* **7**, 345–349 (2014).
31. Rasmijn, L. M. et al. Future equivalent of 2010 Russian heatwave intensified by weakening soil moisture constraints. *Nat. Clim. Change* **8**, 381–385 (2018).

32. Dirmeyer, P. A., Balsamo, G., Blyth, E. M., Morrison, R. & Cooper, H. M. Land–atmosphere interactions exacerbated the drought and heatwave over northern Europe during summer 2018. *AGU Adv.* **2**, e2020AV000283 (2021).
33. Seneviratne, S. I. et al. Investigating soil moisture–climate interactions in a changing climate: a review. *Earth Sci. Rev.* **99**, 125–161 (2010).
34. Koster, R. D. et al. Regions of strong coupling between soil moisture and precipitation. *Science* **305**, 1138–1140 (2004).
35. Cook, B. I., Smerdon, J. E., Seager, R. & Coats, S. Global warming and 21st century drying. *Clim. Dynam.* **43**, 2607–2627 (2014).
36. Cook, B. I., Ault, T. R. & Smerdon, J. E. Unprecedented 21st century drought risk in the American Southwest and Central Plains. *Sci. Adv.* **1**, e1400082 (2015).
37. Dirmeyer, P. A. et al. Projections of the shifting envelope of water cycle variability. *Clim. Change* **136**, 587–600 (2016).
38. Seneviratne, S. I., Lüthi, D., Litschi, M. & Schär, C. Land–atmosphere coupling and climate change in Europe. *Nature* **443**, 205–209 (2006).
39. Petoukhov, V. et al. Alberta wildfire 2016: apt contribution from anomalous planetary wave dynamics. *Sci. Rep.* **8**, 12375 (2018).
40. Teng, H. & Branstator, G. Amplification of waveguide teleconnections in the boreal summer. *Curr. Clim. Change Rep.* **5**, 421–432 (2019).
41. Neal, E., Huang, C. S. Y. & Nakamura, N. The 2021 Pacific Northwest heat wave and associated blocking: meteorology and the role of an upstream cyclone as a diabatic source of wave activity. *Geophys. Res. Lett.* **49**, e2021GL097699 (2022).
42. Wang, J. et al. Changing lengths of the four seasons by global warming. *Geophys. Res. Lett.* **48**, e2020GL091753 (2021).
43. Berg, A. et al. Impact of soil moisture–atmosphere interactions on surface temperature distribution. *J. Clim.* **27**, 7976–7993 (2014).
44. Swain, D. L., Singh, D., Touma, D. & Diffenbaugh, N. S. Attributing extreme events to climate change: a new frontier in a warming world. *One Earth* **2**, 522–527 (2020).
45. van Oldenborgh, G. J. et al. Pathways and pitfalls in extreme event attribution. *Clim. Change* **166**, 13 (2021).
46. Philip, S. et al. A protocol for probabilistic extreme event attribution analyses. *Adv. Stat. Climatol. Meteorol. Oceanogr.* **6**, 177–203 (2020).
47. McKinnon, K. A., Rhines, A., Tingley, M. P. & Huybers, P. The changing shape of Northern Hemisphere summer temperature distributions. *J. Geophys. Res.* **121**, 8849–8868 (2016).
48. Volodin, E. M. & Yurova, A. Y. Summer temperature standard deviation, skewness and strong positive temperature anomalies in the present day climate and under global warming conditions. *Clim. Dynam.* **40**, 1387–1398 (2013).
49. Philip, S. Y. et al. Rapid attribution analysis of the extraordinary heatwave on the Pacific Coast of the US and Canada June 2021. Preprint at *Earth Syst. Dynam*. https://doi.org/10.5194/esd-2021-90 (2021).
50. White, R. H., Kornhuber, K., Martius, O. & Wirth, V. From atmospheric waves to heatwaves: a waveguide perspective for understanding and predicting concurrent, persistent and extreme extratropical weather. *Bull. Am. Meteorol. Soc.* **103**, E923–E935 (2021).
51. Xu, P. et al. Amplified waveguide teleconnections along the polar front jet favor summer temperature extremes over northern Eurasia. *Geophys. Res. Lett.* **48**, e2021GL093735 (2021).
52. Liu, Y., Sun, C. & Li, J. The boreal summer zonal wavenumber-3 trend pattern and its connection with surface enhanced warming. *J. Clim.* **35**, 833–850 (2022).
53. Sun, X. et al. Enhanced jet stream waviness induced by suppressed tropical Pacific convection during boreal summer. *Nat. Commun.* **13**, 1288 (2022).
54. Dirmeyer, P. A. The terrestrial segment of soil moisture–climate coupling. *Geophys. Res. Lett.* **38**, L16702 (2011).
55. Schwingshackl, C., Hirschi, M. & Seneviratne, S. I. Quantifying spatiotemporal variations of soil moisture control on surface energy balance and near-surface air temperature. *J. Clim.* **30**, 7105–7124 (2017).
56. Mueller, B. & Seneviratne, S. I. Hot days induced by precipitation deficits at the global scale. *Proc. Natl Acad. Sci. USA* **109**, 12398–12403 (2012).

Methods

Reanalysis data

All reanalysis data are provided by ERA5 (ref. [57]) of ECMWF, obtained at ~0.25° and 6-hourly resolution; all analyses involve daily or longer means.

Model data

The model experiment we present in Fig. 3b,c is referred to as CAM5–GOGA[58,59]. The atmospheric model is CAM5 (National Center for Atmospheric Research Community Atmosphere Model, v.5.3), which is the atmospheric component of the Community Earth System Model v.1.2 (ref. [60]) at T42 spectral (~2.75°) resolution. The GOGA (Global Ocean Global Atmosphere) experiment involves forcing 16 members of CAM5 with historical monthly sea surface temperatures (HadISSTv.2; ref. [61]) over the period 1856–2014. GHGs and radiative forcing are fixed (GHGs at 2000 levels) and sea ice concentration follows HadISSTv.2. One 16-member ensemble allows soil moisture to interact with the atmospheric model, while the other prescribes soil moisture as the monthly climatology over 1950–2015 at each location derived from all members. We begin analysis in 1870 to avoid model spin-up effects and discard two full members and all years after 2010 due to data discrepancies, resulting in a 14-member by two-ensemble by 141-year dataset. For comparison with reanalysis, we standardize all anomalies on the basis of the 1981–2010 climatology across all grouped prescribed members. We note a caveat that, in this experimental design, water is not strictly conserved in the prescribed soil moisture case, as noted for GLACE-CMIP5 models[43,62,63]—however, an analysis of the resulting water balance perturbation in the CESM model[62] shows that the perturbation is small in the PNW relative to other global regions.

Future GMST trajectories in Fig. 4c are based on decadal-mean Coupled Model Intercomparison Project Phase 6 (CMIP6) multimodel mean anomalies from the pre-industrial period (1850–1900), using all models available (42 for SSP 2–4.5, 35 for SSP 3–7.0 and 44 for SSP 5–8.5 (ref. [64])).

Planetary wave analysis

We apply a Fourier transform to 15-d running means of 300 hPa meridional wind averaged over 37.5–52.5° N, obtaining amplitudes and phase positions of the circulation components of zonal wavenumbers $k = 1$–9. Amplitudes are compared with a monthly climatology over 1981–2010 to calculate standardized anomalies.

Extreme value analysis

Our estimates of likelihoods and return periods of extreme temperatures are derived by fitting GEV distributions to both observational (ERA5) and model data, following widely used procedures designed for investigating extreme events rather than the body of distributions[44–46,49,65]. For all GEV analyses we use the Python package climextRemes[66].

For observations, we first calculate the maximum daily-mean PNW-mean temperature anomaly over June–August each year since 1950 using the ERA5 back extension[67]. We fit a GEV function with non-stationary location and scale parameters (as in ref. [15]) to both datasets 1950–2020 and 1950–2021. Both non-stationary parameters use 5-year smoothed annual-mean GMST as a covariate, provided by NASA's GISTEMP[68]. For both datasets, the addition of non-stationarity in the scale parameter improves the model fit over a stationary-scale fit, based on a likelihood ratio test (significant at the $P < 0.025$ level for the 1950–2021 dataset but with $P = 0.267$ for 1950–2020; Supplementary Table 1) and on comparing Kolmogorov–Smirnov test statistics (Supplementary Figs. 9 and 10). A comparison of the GEV fits against empirical temperature return periods in 1950–1985 versus 1986–2021 visually supports a potential widening (Fig. 4b and Supplementary Fig. 9). Moreover, as such non-stationarity would reflect a variability change rather than a mean shift, it may be physically justified by observed increases in regional temperature skewness since 1979, particularly in June (Extended Data Fig. 6 and Supplementary Fig. 11). The shape parameter, however, is kept stationary: it corresponds to the shape of the upper tail of the GEV and a negative value (as found) indicates a fixed upper bound determining the highest temperature anomaly possible at a given global temperature, which is likely to be true on the basis of energetic constraints.

For model data, we calculate the maximum June mean among all 14 ensemble members for each year. We fit a GEV to these ensemble-maximum June means over 1870–2010, with non-stationary location parameter using 5-year smoothed annual PNWMST as a covariate. Non-stationarity in GMST does not significantly improve the fits over total stationarity, while non-stationarity in PNWMST does ($P < 0.1$ and $P < 0.001$ for prescribed and interactive soil moisture ensembles, respectively, on the basis of a likelihood ratio test). Fits are presented in Fig. 3 evaluated at the annual PNWMST of 2020 (calculated from ERA5) to provide present-day estimates of the 2021 event return periods while minimizing its influence on the PNWMST itself. We repeat the analysis with block sizes of 28 and 42 member-years (finding maxima over 2 and 3 years of data, respectively) and find fairly consistent results but with drastically increased uncertainty as the total block number decreases.

For all GEV results, 95% CIs surrounding return period curves are shown based on a bootstrapping method, as a non-parametric alternative to a parametric method using asymptotic standard errors. Bootstrapping is done with a block size of 1 year and is obtained by resampling (drawing n out of a given n datapoints with replacement, for 5,000 iterations for model data and 1,000 iterations for observational data) and calculating the desired output (return periods as a function of return level) for each iteration. The displayed 95% CI bounds are taken as the 2.5th and 97.5th percentiles of the resulting return period curves. (Bootstrapping in Fig. 2 is also done with a 1-year block size and 5,000 iterations).

Data availability

All ERA5 output data used in this study are available from ECMWF at https://cds.climate.copernicus.eu/cdsapp#!/dataset/reanalysis-era5-single-levels. All CAM5_GOGA output used in this study is available at https://doi.org/10.5281/zenodo.5800726. CMIP6 multimodel mean warming levels are available at https://doi.org/10.5281/zenodo.4600695.

Code availability

All figures were produced using Python v.3.6 (https://www.python.org/downloads/release/python-360/). All code needed to reproduce the main figures is available at https://doi.org/10.5281/zenodo.7153416 (ref. [69]).

References

57. Hersbach, H. et al. The ERA5 global reanalysis. *Q. J. Roy. Meteor. Soc.* **146**, 1999–2049 (2020).
58. Lee, D. E., Ting, M., Vigaud, N., Kushnir, Y. & Barnston, A. G. Atlantic multidecadal variability as a modulator of precipitation variability in the Southwest United States. *J. Clim.* **31**, 5525–5542 (2018).
59. Pomposi, C., Giannini, A., Kushnir, Y. & Lee, D. E. Understanding Pacific Ocean influence on interannual precipitation variability in the Sahel. *Geophys. Res. Lett.* **43**, 9234–9242 (2016).
60. Neale, R. B. et al. The mean climate of the Community Atmosphere Model (CAM4) in forced SST and fully coupled experiments. *J. Clim.* **26**, 5150–5168 (2013).
61. Titchner, H. A. & Rayner, N. A. The Met Office Hadley Centre sea ice and sea surface temperature data set, version 2: 1. Sea ice concentrations. *J. Geophys. Res.* **119**, 2864–2889 (2014).

62. Hauser, M., Orth, R. & Seneviratne, S. I. Investigating soil moisture–climate interactions with prescribed soil moisture experiments: an assessment with the Community Earth System Model (version 1.2). *Geosci. Mod. Dev.* **10**, 1665–1677 (2017).
63. Humphrey, V. et al. Soil moisture–atmosphere feedback dominates land carbon uptake variability. *Nature* **592**, 65–69 (2021).
64. Hauser, M. mathause/cmip_temperatures: version 0.2.1. Zenodo https://doi.org/10.5281/zenodo.5532894 (2021).
65. Coles, S. *An Introduction to Statistical Modeling of Extreme Values* (Springer, 2001).
66. Paciorek, C. climextRemes: tools for analyzing climate extremes. Zenodo https://doi.org/10.5281/zenodo.3240582 (2019).
67. Bell, B. et al. The ERA5 global reanalysis: preliminary extension to 1950. *Q. J. Roy. Meteor. Soc.* **147**, 4186–4227 (2021).
68. *Data. GISS: GISS surface temperature analysis (GISTEMP v4)* (NASA, accessed January 2022); https://data.giss.nasa.gov/gistemp/
69. Bartusek, S. sambartusek/PNW_heatwave_2021: PNW_heatwave_2021. Zenodo https://doi.org/10.5281/ZENODO.7153416 (2022).

Acknowledgements

We are thankful to Y. Wu, R. Horton, D. Singh, C. Raymond, C. Rogers and R. Seager for valuable feedback on this work. We thank D. Lee for configuring, running and making output available from CAM5–GOGA. Support for this work was provided by NSF-AGS-1934358 (S.B., K.K. and M.T.) and NOAA NA20OAR4310379 (M.T.).

Author contributions

M.T. initiated and supervised the project. S.B. and K.K. analysed data with input from M.T. S.B. generated figures and wrote the first draft of the manuscript with input from K.K. and M.T. All authors discussed and edited the manuscript.

Competing interests

The authors declare no competing interests.

Additional information

Extended data is available for this paper at https://doi.org/10.1038/s41558-022-01520-4.

Supplementary information The online version contains supplementary material available at https://doi.org/10.1038/s41558-022-01520-4.

Correspondence and requests for materials should be addressed to Samuel Bartusek.

Peer review information *Nature Climate Change* thanks Rong Fu, Mark Risser and the other, anonymous, reviewer(s) for their contribution to the peer review of this work.

https://doi.org/10.1038/s41558-022-01520-4

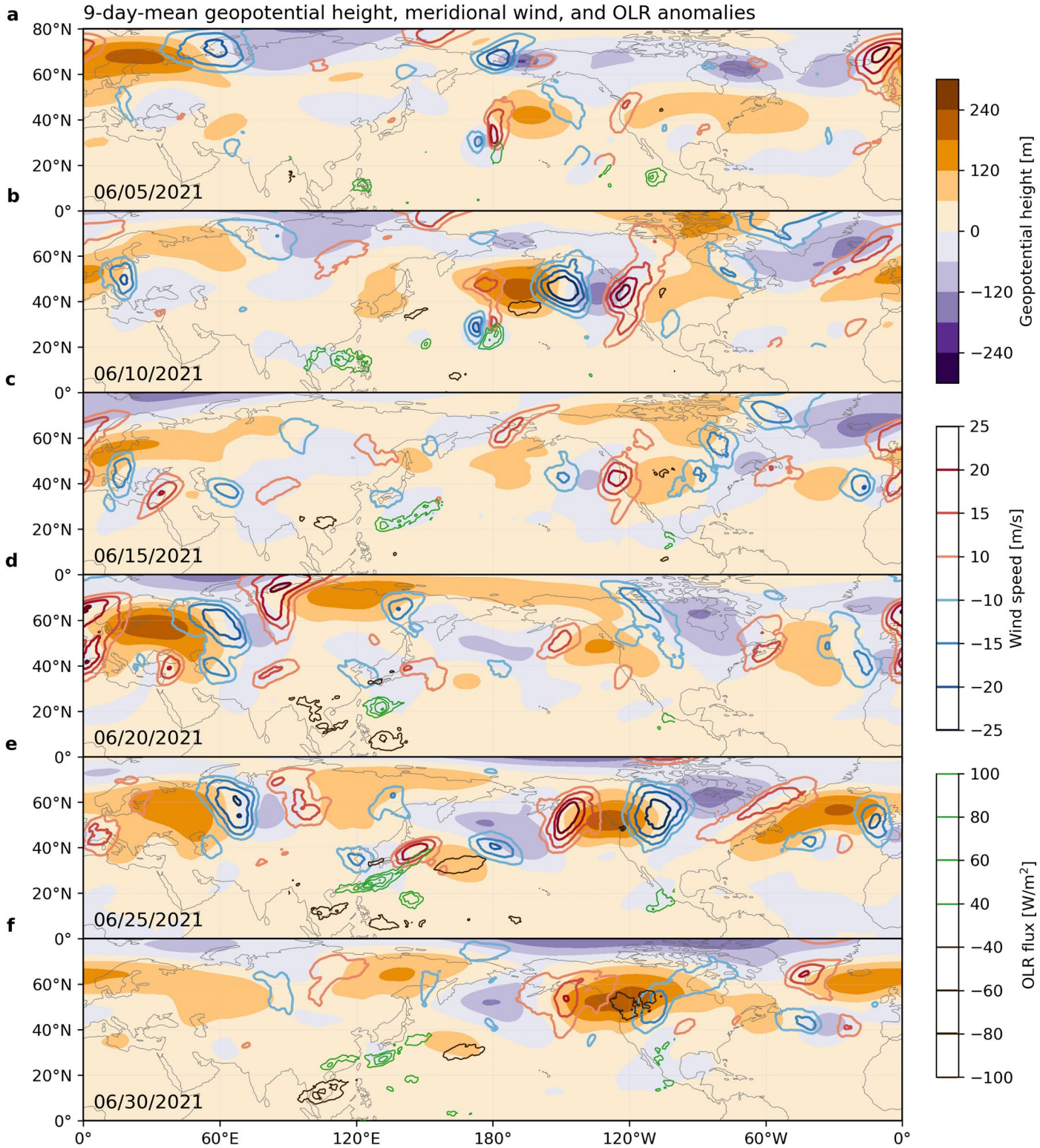

Extended Data Fig. 1 | Atmospheric dynamics during June 2021 leading to the anomalous geopotential heights associated with the PNW heatwave. See Text S1 for further discussion. (**a**–**f**): 500hPa Geopotential height (filled contours), 300hPa meridional wind speed (red and blue contours), and outgoing longwave radiation (OLR; green and dark brown contours) anomalies averaged over 9-day periods centred on the annotated date. For clarity, the meridional wind field is only shown poleward of 20°N and the OLR field is only shown within 90°E–100°W (roughly the Pacific Ocean). For example, (**a**) shows the 9-day mean surrounding 06/05, when geopotential heights were high in the PNW accompanying a heatwave, with centres of low and high geopotential height extending westward over the Pacific forming a tripole. By 06/10 (**b**)) the tripole had expanded longitudinally, placing negative geopotential height over the PNW, and begun to constitute part of a wavenumber-4 pattern in meridional wind and geopotential height encircling the midlatitudes. Over 06/10–06/20 (**c**–**e**)) this wavenumber-4 pattern moved slightly northward and shifted phase longitudinally, eventually placing high geopotential height over the PNW. Throughout the last two weeks of June (**d**–**f**)) the wavenumber-4 pattern persisted and amplified, causing extreme temperatures and dry soils in central Europe, Siberia, and the PNW, and was reinforced by a Rossby wavetrain emanating from the subtropical western Pacific.

https://doi.org/10.1038/s41558-022-01520-4

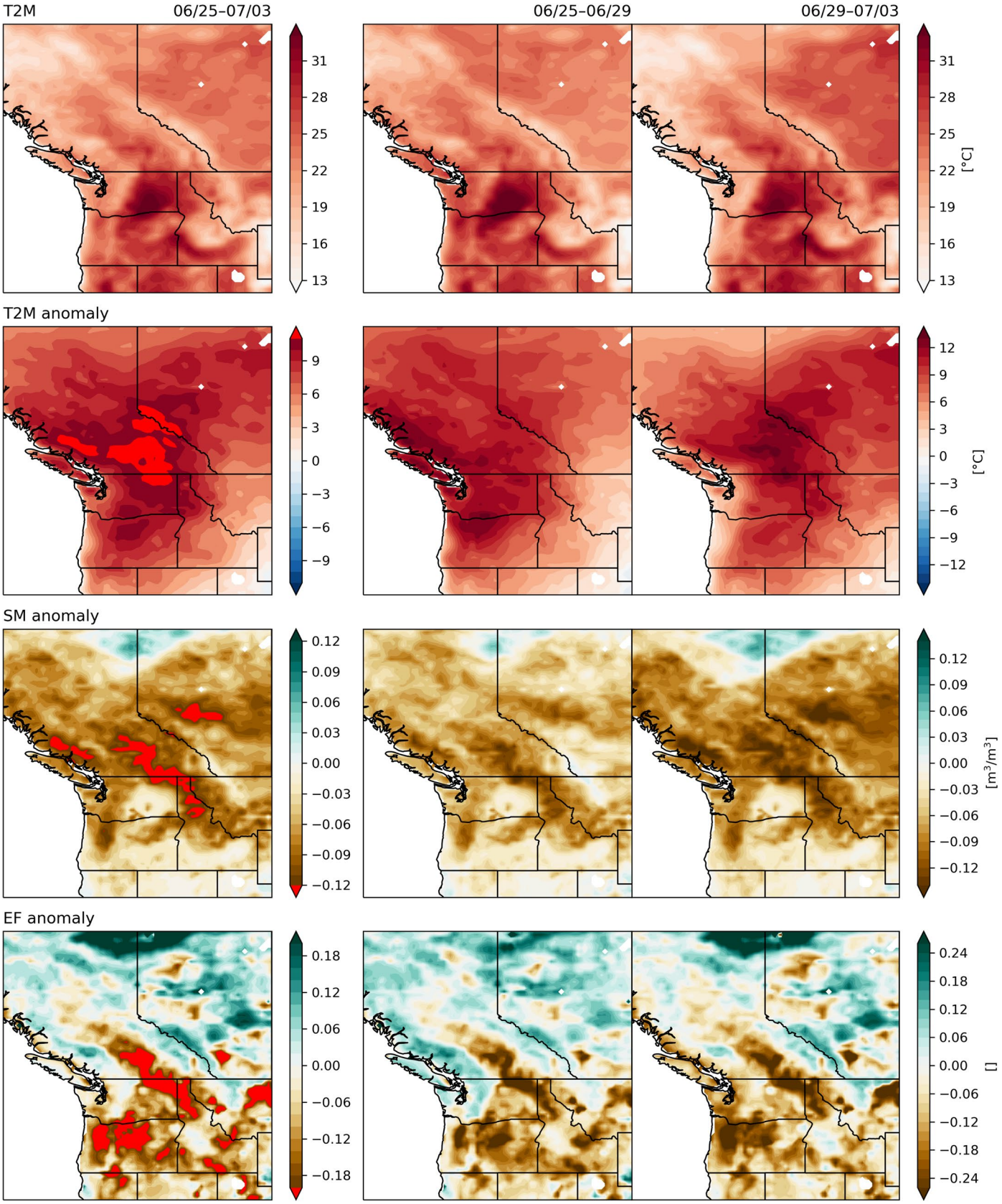

Extended Data Fig. 2 | See next page for caption.

https://doi.org/10.1038/s41558-022-01520-4

Extended Data Fig. 2 | PNW land–atmosphere anomalies during the 2021 heatwave. Mean conditions over the whole 9-day heatwave period (06/25–07/03; **left column**), its first half (06/25–06/29; **middle column**), and its second half (06/29–07/03; **right column**), for 2 m temperature (T2M) (**top row**), T2M anomalies (**second row**), soil moisture (SM) anomalies (**third row**), and evaporative fraction (EF) anomalies (**bottom row**). EF is calculated from daily-mean latent heat flux (LHF) and sensible heat flux (SHF) as LHF/(SHF + LHF). Many of the regions of hottest (absolute) T2M and hottest T2M, driest SM, and lowest EF (high SHF vs. total HF) anomalies during this heatwave overlapped, particularly in the center of the region: across northern Oregon, eastern Washington, northern Idaho, and central southern British Columbia (the Interior Plateau). However, some of the largest T2M anomalies were associated with high EF (high LHF vs. total HF) anomalies instead—mostly in the Coastal and Cascade mountains on the British Columbia coast and the Cariboo and Monashee mountains between British Columbia and Alberta. This pattern is very consistent with climatological daily correlation between EF and T2M anomalies (see Extended Data Fig. 6): areas where EF and T2M are anticorrelated (both typically and during this event) tend to be warmer, non-mountain areas with relatively low soil moisture and more arid and/or Mediterranean continental climates (that is, across much of eastern Oregon and Washington (the Columbia Plateau), Idaho, and British Columbia's Interior Plateau. Therefore, overall, throughout the heatwave (06/25–07/03), the spatial anticorrelation between EF and T2M anomalies was very weak, reflecting the diversity of land types and land–atmosphere coupling regimes across the large region (yielding $r = -0.04$). However, where T2M was both anomalously and climatologically high, EF and T2M were more tightly anticorrelated. Masking to retain only land regions under the 850hPa level, the spatial correlation was −0.24, with $p < 0.0001$ (significance tested non-parametrically, accounting for spatial autocorrelation).

https://doi.org/10.1038/s41558-022-01520-4

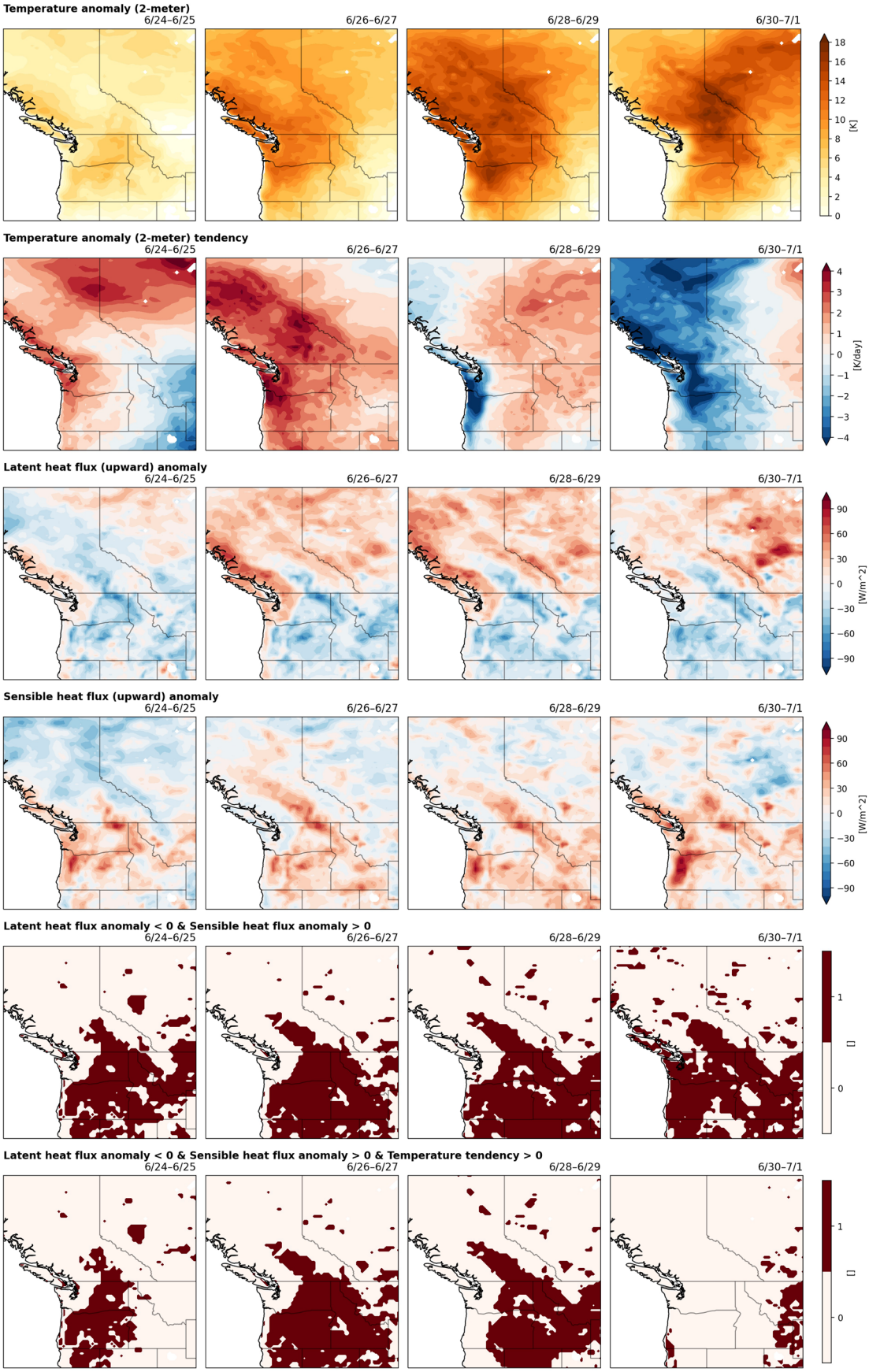

Extended Data Fig. 3 | 2-metre temperature anomaly, tendency, and latent versus sensible heat flux partitioning. Two-day averages throughout 6/24–7/1, focusing on the heating phase of the event. The second-to-last row identifies points where the two-day average upward latent heat flux (LHF) was diminished and sensible heat flux (SHF) was enhanced (exhibiting negative and positive anomalies relative to 1981–2010, respectively, which tended to show strong persistence throughout the season). The last row further subselects points where the temperature tendency was also positive.

https://doi.org/10.1038/s41558-022-01520-4

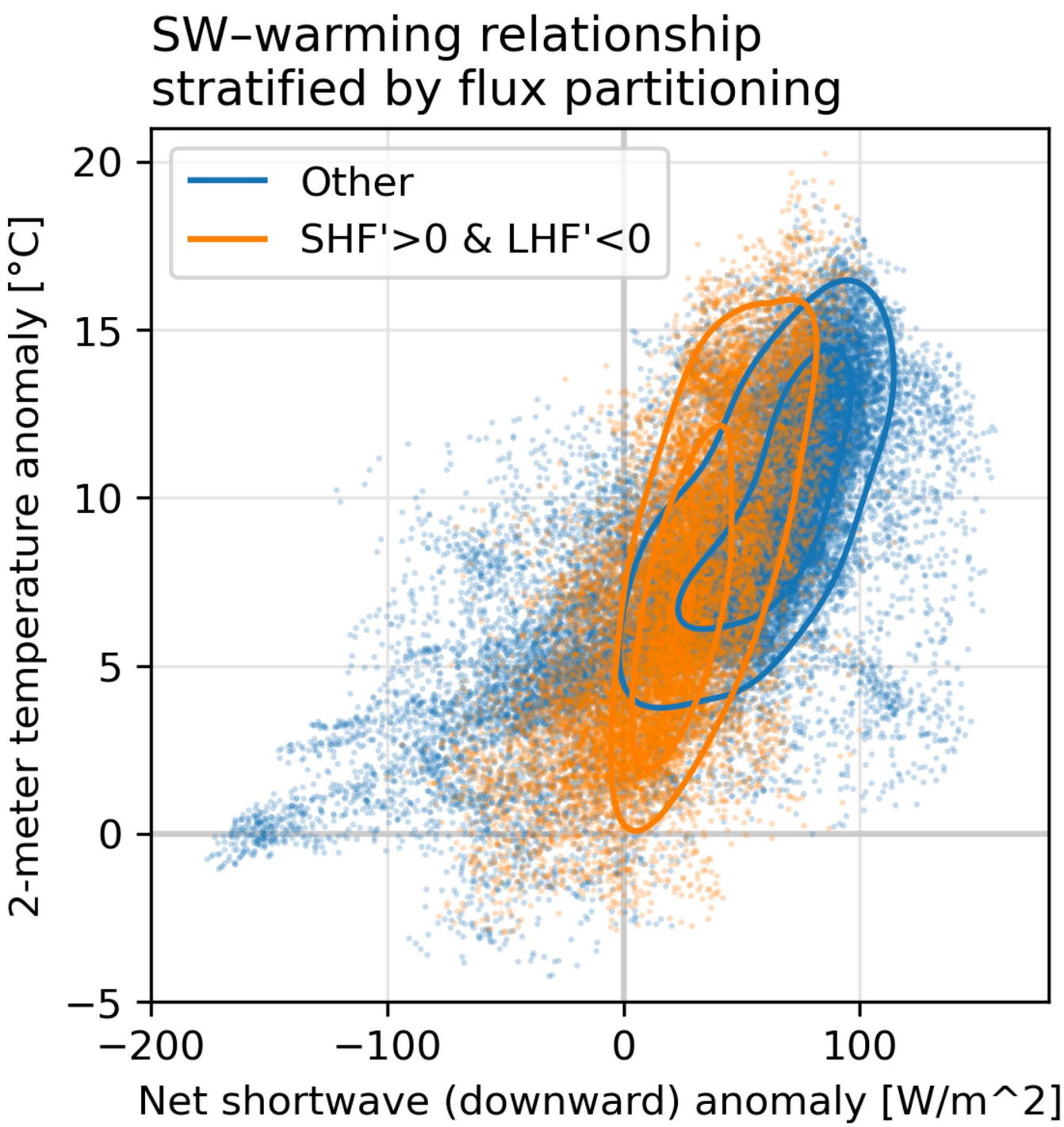

Extended Data Fig. 4 | SW–warming relationship stratified by flux partitioning. Points are daily averages for each land gridcell in the PNW region, over the heatwave period (06/25–07/02), with net SW (downward) anomaly plotted against 2-metre temperature anomaly. Orange dots represent daily averages at each point within the evolving mask shown in the second-to-last row of Extended Data Fig. 3, that is where (upward) sensible heat flux (SHF) was enhanced and latent heat flux (LHF) was diminished. Blue dots show all other land gridcells in the region. (KDE) contours are shown for each group of gridcells, considering only points with net anomalous shortwave radiation > 0, so that points not relevant to heating do not bias the KDE characterization.

https://doi.org/10.1038/s41558-022-01520-4

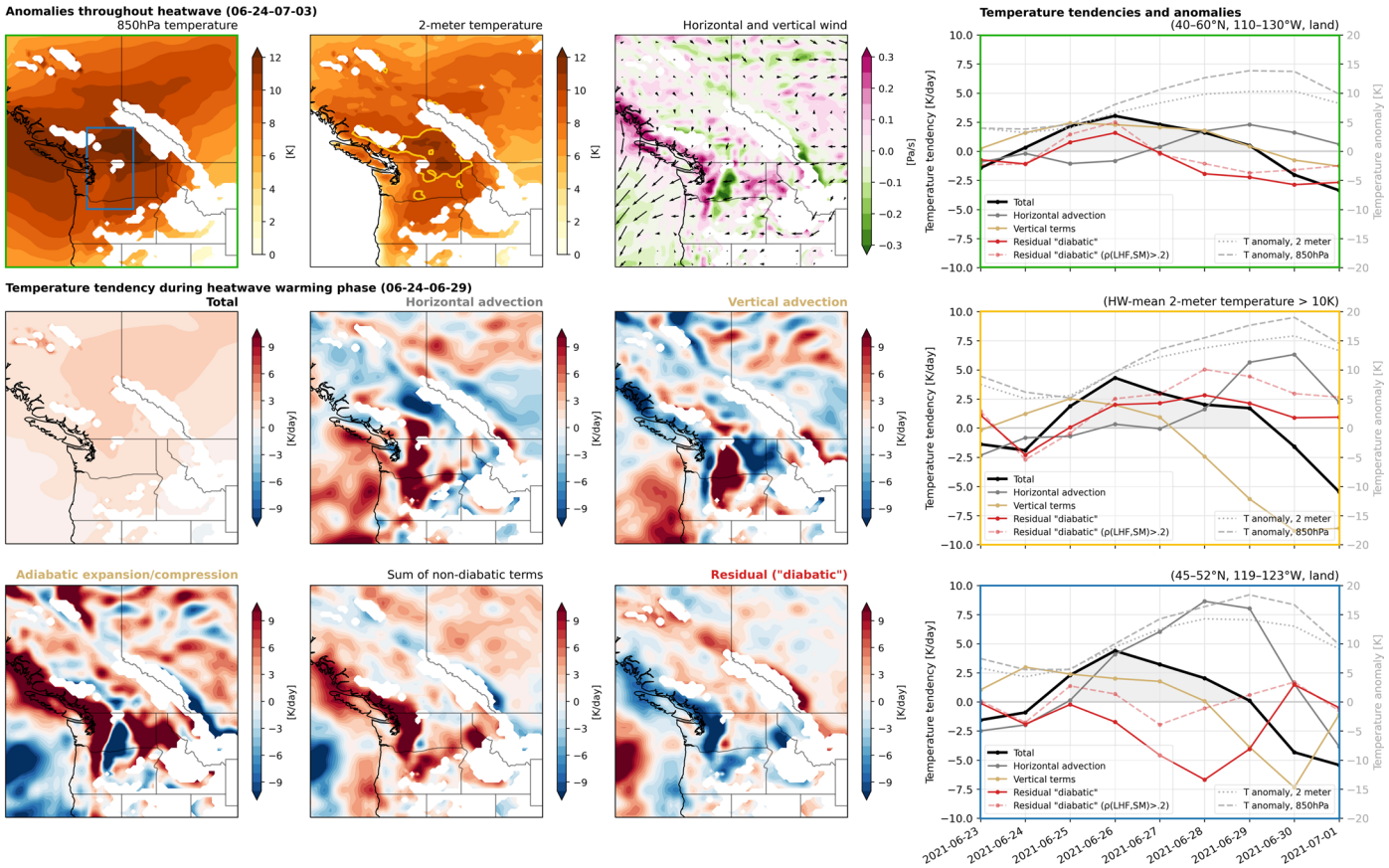

Extended Data Fig. 5 | Temperature tendency budget analysis at 850 hPa. See Text S2 for further discussion. **Top row, left:** Temperature (at 850 hPa and 2 metres) and horizontal and vertical wind (at 850 hPa) anomalies averaged during the 2021 PNW heatwave (06/24–07/03). The green box, blue box, and yellow contour outline the subregions highlighted in the right column (the green box shows the region focused on in the main results). **Bottom two rows, left:** Spatial patterns of contributions from various (grouped) terms in the 850 hPa temperature tendency budget, averaged throughout the heatwave warming phase (06/24–06/29). The residual 'diabatic' term is calculated as the total tendency minus the sum of all non-diabatic terms, and indicates processes not accounted for by the non-diabatic terms that may in part be attributed to land–atmosphere processes. Fields are smoothed with a running 4-gridcell (~1°) window in both directions. **Right column:** Temporal evolution of grouped terms in the budget throughout 06/23–07/01, averaged within the green, yellow, and blue outlined areas (in top row of maps). Solid lines show the total heating, horizontal heat advection, the sum of vertical heat advection and adiabatic expansion/compression, and the residual term. Additionally, the dashed translucent red line shows the residual term only where the long-term daily correlation between latent heat flux (LHF) and soil moisture (SM) exceeds 0.2 (see Extended Data Fig. 6), that is, where land–atmosphere interactions may be more likely to cause positive feedbacks on temperature extremes. 2-metre and 850hPa temperature anomalies in each sub-region are shown on the right axes.

https://doi.org/10.1038/s41558-022-01520-4

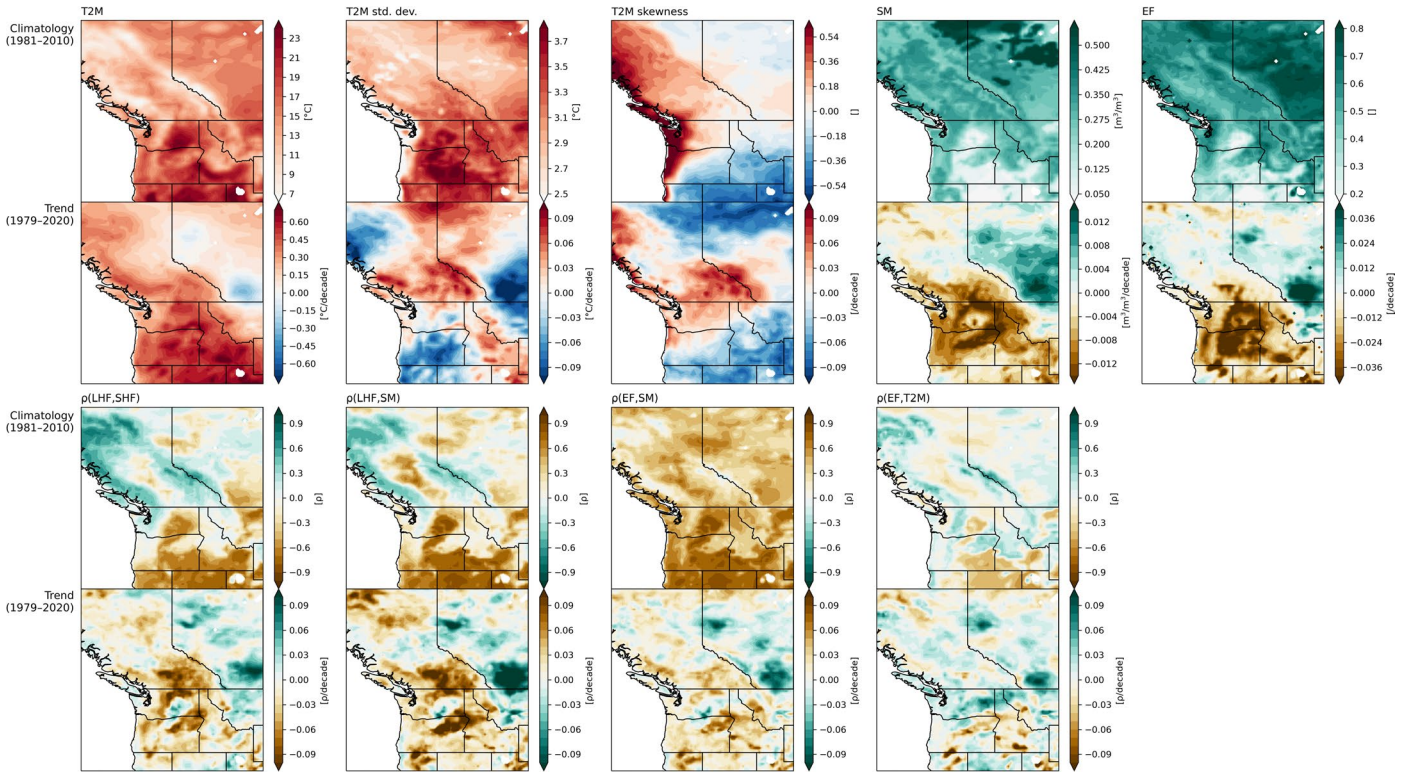

Extended Data Fig. 6 | Climatologies and trends of PNW temperature variability and land–atmosphere quantities. Top row: 1981–2010 June–July climatologies (top panels) and 1979–2020 linear trends (bottom panels) of 2 m temperature (T2M), T2M variability (within-year standard deviation and skewness of daily anomalies), soil moisture (SM), and evaporative fraction (EF, calculated from daily latent heat flux [LHF] and sensible heat flux [SHF] as LHF/[LHF + SHF]). **Bottom row:** Climatologies and trends of four metrics of land–atmosphere coupling: the first three (correlations between LHF and SHF, LHF and SM, and EF and SM) represent the terrestrial component, while EF and T2M correlation represents the total feedback pathway. Correlation climatologies are created by correlating two variables (with June–July 1979–2020 trends removed) against each other throughout all June–July 1981–2010 days. Trends are between correlations within June–July of individual years (1979–2020). While SM and T2M are nearly everywhere anticorrelated, these metrics show where soil moisture deficit may causally affect T2M: LHF/SHF anticorrelation, LHF/SM correlation, EF/SM correlation, and EF/T2M anticorrelation indicate moisture-limited (versus energy-limited) regimes with potentially stronger land–atmosphere coupling, typical of transitional climate zones. If evapotranspiration is moisture-limited, under heating EF may decrease (SHF's partition of flux increases), allowing for positive land–atmosphere feedbacks by further increasing T2M, decreasing SM, increasing SHF and decreasing LHF. Climatologically, such areas extend from the drier interior central West to the Columbia Plateau in eastern Washington and into interior British Columbia (bottom row, top panels). Trends indicate that much of the PNW has undergone strengthening in at least the terrestrial component of land–atmosphere coupling—most notably where soil moisture is climatologically moderate as opposed to extremely low, including much of BC's Interior Plateau, much of the Cascade Range region (including near Portland and Seattle) and to the east of the Columbia Plateau. In some of these areas, T2M itself has become more coupled to EF, potentially signifying strengthened feedbacks—but such trends have not conclusively emerged overall. The spatial pattern of strengthening land–atmosphere coupling corresponds relatively well with warming, drying, and decreasing EF, and in some places with increasing T2M variability (areas of increasing T2M standard deviation and skewness correspond better to land–atmosphere correlation trends than to SM or EF trends alone).

https://doi.org/10.1038/s41558-022-01520-4

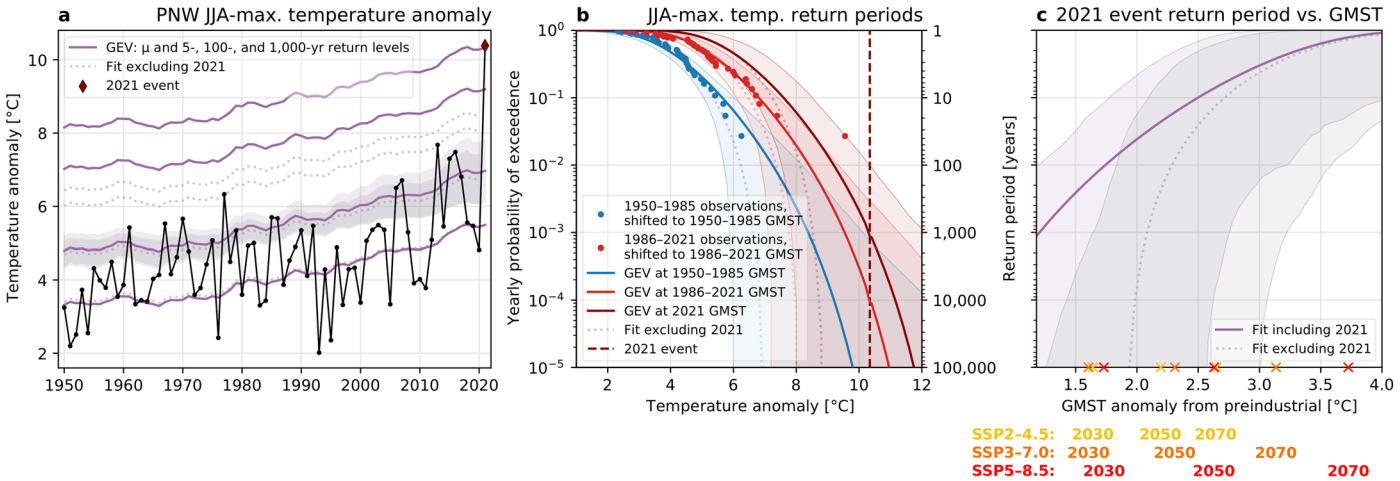

Extended Data Fig. 7 | Fit and validation for non-stationary location, stationary-scale historical GEV fit. Same as Fig. 4 but showing results from a GEV distribution fit with stationary-scale parameter (location parameter is still non-stationary). Bootstrapped 95% confidence intervals are shaded as in Fig. 4.